Pergamon

Available online at www.sciencedirect.com
SCIENCE DIRECT®

Cement and Concrete Research 33 (2003) 1155–1173

CEMENT AND CONCRETE RESEARCH

Poroplastic properties of calcium-leached cement-based materials

Franz H. Heukamp, Franz-Josef Ulm*, John T. Germaine

Massachusetts Institute of Technology, Cambridge, MA 02139, USA

Received 4 December 2001; accepted 10 January 2003

Abstract

Asymptotic calcium leaching of cement-based materials produces a new material composed of C–S–H with low *C*/*S* ratio on the order of 1 and a high porosity generated by the dissolution of Portlandite (CH) crystals, which creates a new pore-size family in the micrometer range. This paper investigates the role of these two phenomena in the multiaxial inelastic and hardening deformation behavior, in compression, of calcium-leached cement pastes and mortars. From triaxial tests and SEM microscopy, it is shown that the low *C*/*S* C–S–H matrix is highly plastically deformable, which is consistent with the high degree of polymerization and the effect of the *C*/*S* ratio on the intrinsic cohesion of C–S–H. The validity of the effective stress concept is experimentally proven for calcium-leached cement paste and mortar and provides evidence that the low *C*/*S* C–S–H solid phase of the cement paste is a pure cohesive incompressible material. In turn, the large pores created by the CH dissolution provides expansion space for the incompressible solid during compressive loading. Once this porosity is filled, the volume deformability is exhausted, and the material dilates to failure. In a similar way, the early tendency of mortars to dilate is found to be a consequence of a competition between plastic material behavior of the matrix (plastic hardening) and porosity-controlled structural deformation (geometrical hardening) triggered by frictional dilation mechanisms in the Interfacial Transition Zone (ITZ).

Keywords: Durability; Mechanical properties; Degradation; SEM; Interfacial Transition Zone; Poromechanics

1. Introduction

The durability of concrete structures used in long-term applications such as nuclear waste containment structures, dams, pipes, water storage tanks, and tunnels is of importance for their safe and efficient operation. To preserve the functionality of a given structure, so that its mechanical performance meets the requirements of its usage at all times, is the goal of durability design. Durability design itself is based on the intimate knowledge of the evolution of the mechanical properties in material degradation processes.

Calcium leaching-induced aging is among the possible degradation scenarios of concrete. Calcium leaching of cementitious materials creates a new material. The study of the mechanical properties of this new material supplies the information needed for durability design. In this study, the multiaxial strength and deformation behavior, both key properties for the integrity and functionality of structures, are investigated.

Calcium leaching occurs when cementitious materials are exposed to water with calcium concentrations below the equilibrium concentration. Following the equilibrium conditions in the system $CaO–SiO_2–H_2O$ [1],[1] first, the Portlandite [$CH = Ca(OH)_2$] is dissolved, and then the C–S–H are decalcified, reducing their *C*/*S* ratio. The polymerization of C–S–H is known to increase with decreasing *C*/*S* ratios [2], and an increase in the relative chain length during calcium leaching was reported from nuclear magnetic resonance studies by Porteneuve [3]. Adenot [4] showed that the leaching process is governed by the diffusion of calcium in the attacking water phase, and developed a 1D-model which accounts for the experimentally observed instantaneous dissolution of the distinct mineral phases. This work was extended by Mainguy et al. [5–7] for two-dimensional problems and cracked materials. The critical importance of the diffusion process for the kinetics of the leaching process was the basis for the development of accelerated leaching techniques: replacing water with an ammonium nitrate solution was first introduced by Carde, while an electro-

* Corresponding author. Tel.: +1-617-253-3544; fax: +1-617-253-6044.
E-mail address: ulm@mit.edu (F.-J. Ulm).
URL: http://cist.mit.edu.

[1] Cement chemistry notation used throughout: C = CaO; S = SiO_2; H = H_2O.

0008-8846/03/$ – see front matter © 2003 Elsevier Science Ltd. All rights reserved.
doi:10.1016/S0008-8846(03)00024-3

chemically induced leaching process was pioneered by Saito et al. [8] and Gérard [9]. While the ammonium nitrate solution achieves an acceleration of the leaching process due to the increased calcium concentration gradient in the attacking fluid phase, the electrochemical acceleration results from a strong electrical potential difference. The decrease in uniaxial compressive strength with calcium leaching was shown by Carde [10] on laboratory specimens, and the detrimental impact of calcium leaching on existing concrete structures was shown by Mason [11], reporting strength degradation in dams, and by Wittmann [12], describing the leaching-induced pathologies of water storage tanks. Structural laboratory tests were performed by Schneider and Chen [13] and Le Bellégo [14] on mortar beams. The first tested beams under ongoing decalcification and determined residual flexural strength, and Le Bellégo presented results on three point-bending tests of notched beams of different sizes under ongoing decalcification and studied size effects induced by calcium leaching. The degradation of the material stiffness and uniaxial strength was modeled by Carde [10], Gérard [9] and Le Bellégo [14] using damage models, and by Ulm et al. [15] using a chemoplastic softening model. A first study of the evolution of the triaxial strength domain and the pressure sensitivity of calcium-leached cement pastes was presented recently [16].

It is now well known that the material properties of decalcified cement pastes and mortars depend on the calcium concentration. Due to the diffusion-dominated kinetics of the leaching process, leached specimens, however, always show locally varying calcium concentrations which prohibit a unique conclusion on material properties from mechanical tests. The calcium concentration is uniform only in an intact specimen and in an asymptotically decalcified specimen. These two asymptotic states frame all physical states of cement-based materials subjected to calcium leaching. Focus of this paper is the characterization of the mechanical properties of homogeneously decalcified cement-based materials, namely, cement paste and mortar, obtained by leaching in a 6 M ammonium nitrate solution.

2. Materials, test setup, and analytical framework

2.1. Material and specimen preparation

The cement pastes and mortars were prepared at a water–cement ratio $w/c = 0.5$, using an ordinary Type I Portland cement. The composition of the cement is given in Table 1. The mortar composition is characterized by water–cement–sand mass ratio of $w/c/s = 1{:}2{:}4$, using a fine Nevada sand of density 2650 kg/m^3, $d_{60} = 0.23$ mm and $d_{30} = 0.17$ mm. Both the cement paste and the mortar were cast in cylindrical PVC molds with a diameter of 11.5 mm and a length of 60 mm. The molds were prepared with oil to facilitate the demolding process. After 24 h of curing, the specimens were demolded in a simple pushout procedure and kept in a saturated lime solution at 20 °C until being tested. The rather small specimen size which was chosen to shorten the leaching time still leads to an acceptable variability in material properties. In a series of preliminary compression tests, the variability of the specimens was tested. The relative error was smaller than 6%, which is an acceptable value.

Table 1
Type I Portland cement constituents (in mass%)

OPC type I					
CaO	SiO_2	Al_2O_3	MgO	SO_3	Na_2O
62.3	20.8	4.4	3.8	2.9	0.39
Fe_2O_3	K_2O	C_3Al	C_3S	C_2S	Ignition loss
2.4	1.28	8	53	20	0.66

Data from producer.

After 28 days of curing in lime water, the specimens were subjected to accelerated calcium leaching using a highly concentrated ammonium nitrate solution (6 M) in a slowly oscillating container, which assures good mixing conditions (for details see Ref. [16]). The measured leaching kinetics were found to be identical for mortar and paste, in accordance with Ref. [17]. The position of the Portlandite dissolution front was found to be governed by a self-similar form $x_d = 2\ \text{mm}/\sqrt{d}$, reaching the sample center after some 9 days (the diameter being 11.5 mm). Uniformly calcium-leached samples are obtained after some 45 days [16], having a residual calcium concentration of about 10% of the solid mass, and a C/S ratio close to 1, determined from XRF analysis.

The change in porosity with respect to water was measured for unleached and leached cement pastes and mortars (Table 2), involving drying at 105 °C. While this process generally leads to an overestimation of the actual porosity (as parts of the chemically bound water also evaporate), the measurements clearly show that calcium-depleted cementitious materials are extremely porous, which is expected to influence their mechanical behavior decisively.

Based on the density and porosity measurements, the volumetric fraction of sand in the calcium-depleted mortar can be derived to be approximately 50%. Before being tested, the specimens are cut to a length of 23 mm, which corresponds to a height/diameter ratio of 2.

Finally, leached materials before and after hydrostatic compression were investigated with a JEOL 6320FV SEM of the Center of Materials Science and Engineering (CMSE) at MIT. Cylindrical specimens were prepared with polished, epoxy-impregnated surfaces [18]. The finest polishing step was 0.25 μm. Samples were coated with Au–Pd before examination under the SEM. Working distance was around 19 mm, and low voltages (1 kV–5 kV) were used to avoid charging.

Table 2
Material characterization of nondegraded and degraded cement paste and mortar specimens: porosity (accessible to water), density, friction coefficient, and cohesion (Mean ± S.D.)

Specimen	Cement paste		Mortar	
	Nondegraded	Degraded	Nondegraded	Degraded
Initial porosity (%)	39.7 ± 1.1	63.2 ± 1.6	27.5 ± 0.4	40.1 ± 2.4
Density$_{(sat.)}$ (kg/m^3)	1898 ± 9	1351 ± 12	2171 ± 15	1831 ± 19
Friction coefficient α [1]	0.82	0.56	1.02	0.81
Cohesion c (MPa)	17.11	1.15	9.82	0.96

2.2. Triaxial test equipment

The triaxial test device in this study is adapted from common configuration in the MIT Geomechanics Laboratory. In the triaxial test, cylindrical specimens are tested, and a radial stress is applied by a pressurized fluid along with a vertical force. Fig. 1a–c displays the triaxial equipment used in this test series. It consists of a steel chamber filled with silicon oil and seated on a brass base and a steel shaft with an internal load cell on its end (Fig. 1a–b). The movement of the base is controlled and used for displacement-driven tests. The vertical shaft connects through a steel ball on the upper side to the external frame, guaranteeing a moment-free connection (Fig. 1a). The interior of the steel chamber is sealed to the bottom by an O-ring which gets compressed by four bolts that attach the steel chamber to its base. On the top, the shaft passes through an O-ring seal. The details of the specimen connection are shown in Fig. 1c. On the top of the specimen, a half-sphere-shaped steel end connects to the specimen. Its curved side is received by another steel end with a hallow half-sphere shape. The upper steel cap connects to the load cell through a pressure contact. On the bottom of the specimen, a porous stone made of steel is placed. It is there for draining purposes which will be detailed later. The porous stone sits on a hollow steel cylinder. Through this cylinder, an exterior water entrance is connected. The hollow steel cylinder itself is placed in a steel base (see Fig. 1b). The seal is assured by an O-ring in the base. The specimen and the additional elements are placed in a latex tube, and the exterior stress is applied by the oil pressure. The latex membrane is impermeable to oil and water in the specimen.

The change in fluid mass per unit volume, $m_f - m_{f0}$, is measured in the experimental setup at the end of the fluid mass supply tube that connects to the bottom of the specimen. The change in fluid mass is measured as a volume change via an Linear Variable Differential Transformer (LVDT) transducer with infinite resolution. Through the fluid mass supply, the pore pressure p is also measured via a pressure transducer. The oil pressure in the cell is measured with an identical pressure transducer. The imposed vertical displacement δu_z (displacement-controlled test) is measured through an additional LVDT transducer at the bottom of the cell. The characteristics of these devices and of the internal load cell are summarized in Table 3. The high-pressure triaxial test system includes two data acquisition systems. A local system is used for test control purposes, while a central system is used for the data storage. The local system makes use of an analog-to-digital conversion card, which allows the control of the testing procedure

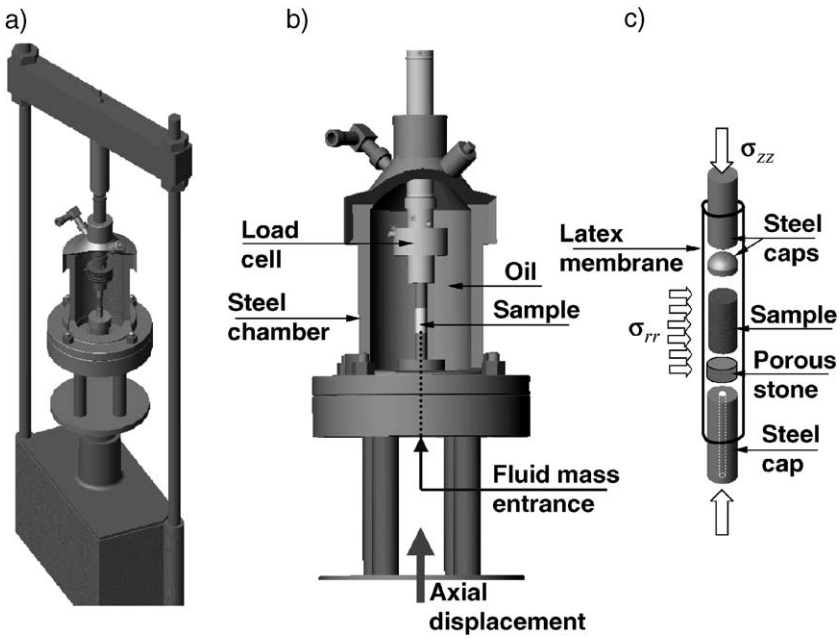

Fig. 1. View of the triaxial cell assembly.

Table 3
Transducer characteristics as measured by the data acquisition system

Device	Range	Resolution	Stability
Axial strain LVDT	5 cm	$\pm 1\times10^{-4}$ (0.1 mV)	$\pm 1\times10^{-3}$ (1 mV)
Volumetric LVDT	45 cm^3	$\pm 1\times10^{-4}$ (0.1 mV)	$\pm 1\times10^{-3}$ (1 mV)
Cell pressure transducer	35 MPa	3×10^{-4} MPa (0.001 mV)	3×10^{-3} MPa (0.01 mV)
Load cell 1	44.59 kN	0.2 N (0.001 mV)	2 N (0.01 mV)
Load cell 2	17.27 kN	0.2 N (0.001 mV)	2 N (0.01 mV)

The resolution and stability calculations for the LVDT are based on dimensions of an average specimen (length 23 mm and diameter 11.5 mm).

using special testing software developed in MIT Geomechanics laboratory [19].

The test device allows carrying out tests under different fluid pressure–fluid mass conditions.

- In a drained test, the pore pressure is kept constant at $p=p_0$, and fluid is extracted from or pushed into the specimen to keep the pressure constant. The corresponding change in fluid mass is recorded and converted into a change in (Lagrangian) porosity according to Ref. [20]:

$$m_f - m_{f0} = \rho_f\phi - \rho_{f0}\phi_0 \tag{1}$$

where m_f and m_{f0} are the current and initial fluid mass per unit initial volume, respectively. ρ_f and ρ_{f0} denote the current and the initial fluid density. In the drained test, $\rho_f(p_0)=\rho_{f0}$, so that the change of porosity $\phi-\phi_0=(m_f-m_{f0})/\rho_{f0}$ is continuously recorded. The Lagrangian porosity ϕ is defined as the ratio of current fluid volume V_f and initial volume V_0 of the specimen:

$$\phi = \frac{V_f}{V_0} = \frac{V - V_s}{V_0} \tag{2}$$

where V is the volume of the specimen in the deformed configuration, and V_s the solid volume in the deformed configuration. The total volume variation of the specimen in a test is due to the change of porosity and the compressibility of the solid phase of the porous material:

$$\frac{V}{V_0} = 1 + \phi - \phi_0 + \frac{V_s - V_{s0}}{V_0} \tag{3}$$

with $V_{s0}=(1-\phi_0)\,V_0$ the initial solid volume.

- In an undrained test, the fluid supply is closed, that is, the change in fluid mass is zero, $m_f=m_{f0}$. The pore pressure can still be measured but because of the deformability of the tubing and transducers and pressure losses at connections, the measured values always underestimate the real fluid pressure in the specimen. Since no change in fluid mass is measured, the change in porosity is not accessible in an undrained test.

2.3. Loading paths in triaxial compression tests

Three types of test were chosen to provide a good scan of the inelastic deformation properties in the stress space.

(1) Hydrostatic compression test; in which the principal stresses are equal to the mean stress $\Sigma_I=\Sigma_{II}=\Sigma_{III}=\Sigma_M=(1/3)\Sigma_{kk}$. In the hydrostatic compression tests, the pore pressure (if any) is prescribed first, and kept constant during subsequent hydrostatic loading. The loading rate is $|\dot{\Sigma}_M|\simeq 5$ kPa/s, which corresponds to strain rates close to $|\dot{E}_{zz}|=5\times10^{-6}\ s^{-1}$, which is required according to consolidation theory to ensure drained conditions for calcium-leached materials (see Appendix A). The maximum applied cell pressure is $\Sigma_M=-10$ MPa.

(2) Deviatoric loading tests at increasing confinement. In these tests, the deviatoric stress, the difference between radial and vertical stress $|\Sigma_{zz}-\Sigma_{rr}|$, is increased at the same time as the confinement, expressed as the negative mean stress, $\bar{p}=-\Sigma_M$, is increased. The loading in the deviatoric tests involves two loading phases: a proportional pore pressure–hydrostatic stress loading is applied first. The pore pressure p is monitored through the fluid mass, and the hydrostatic stress Σ_M^{hyd} through the cell pressure device. The specimen is kept at constant consolidation pressure during 15 h to allow secondary compression to take place. A deviatoric loading path is then applied, during which the cell pressure Σ_{rr} is kept constant, while an additional axial load $\delta F<0$ (δ denotes the change of a parameter after the hydrostatic loading phase) is applied until failure of the specimen. During this second loading phase, the confinement $\bar{p}$ increases, which justifies the naming of the test. The test is performed displacement-driven at a constant axial strain rate of $|\dot{E}_{zz}|=5\times10^{-6}\ s^{-1}$, which allows one to achieve drained conditions during the test (see Appendix A).

(3) Deviatoric loading tests at decreasing confinement, $\bar{p}=-\Sigma_M$. In this kind of test, first a hydrostatic pressure, Σ_M^{hyd}, is applied along with a pore pressure p, identical to the deviatoric loading test at increasing confinement. In the second loading phase, however, a deviatoric load is applied at the same time as the confinement is reduced. This is achieved in a combined deformation–stress-controlled test,

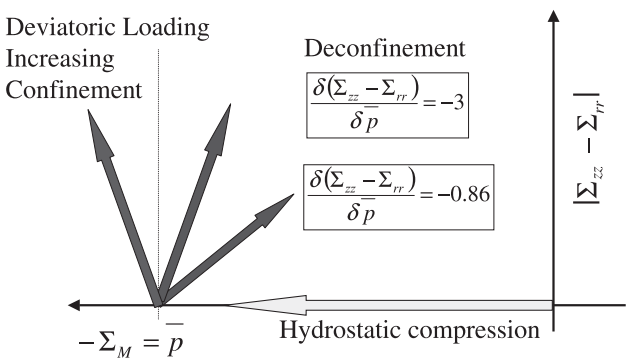

Fig. 2. Schematic representation of the different loading paths in the $|\Sigma_{zz}-\Sigma_{rr}|\times\Sigma_M$ half-plane.

in which the stress ratio $\gamma = \delta(\Sigma_{zz} - \Sigma_{rr})/\delta\bar{p}$ is kept constant. The change in deviatoric stress is provoked by an axial displacement at a rate of $|\dot{E}_{zz}| = 5 \times 10^{-6}\ \mathrm{s}^{-1}$, and the radial stress Σ_{rr} is adjusted via the computer-controlled system to remain on the prescribed loading path. Two stress paths are followed after the hydrostatic compression to $\Sigma_{\mathrm{M}}^{\mathrm{hyd}} \approx -10$ MPa: in the first, the deconfinement ratio is $\gamma = -0.86$; in the second, $\gamma = -3$.

Fig. 2 gives a schematic view of the three test types and their loading paths in the $|\Sigma_{zz} - \Sigma_{rr}| \times \Sigma_{\mathrm{M}}$ half-plane.

2.4. Format of results

The test results are analyzed on the background of the Biot–Coussy theory of porous media [20]. The results are displayed in form of the energy-conjugated stress and deformation quantities, obtained from the external work rate in the triaxial test, which reads (see derivation in Appendix B):

$$\frac{\mathrm{d}W_{\mathrm{ext}}}{\mathrm{d}t} = (\Sigma_{\mathrm{M}} + p)\frac{\mathrm{d}\phi}{\mathrm{d}t}V_0 + (\Sigma_{zz} - \Sigma_{rr})\left(\frac{\mathrm{d}E_{zz}^{\ln}}{\mathrm{d}t} - \frac{1}{3}\frac{\mathrm{d}E_{\mathrm{v}}^{\ln}}{\mathrm{d}t}\right)V \tag{4}$$

The first term in Eq. (4) represents the volumetric work rate provided by the effective stress $\Sigma'_{\mathrm{M}} = \Sigma_{\mathrm{M}} + p$ to the solid phase of the porous material. The second term is a deviator work term associated with shear deformation, where $\mathrm{d}E_{\mathrm{v}}^{\ln} = \mathrm{d}V/V$ and $\mathrm{d}E_{zz}^{\ln} = \mathrm{d}L/L$—in contrast to $\mathrm{d}\phi = \mathrm{d}V_{\mathrm{f}}/V_0$—are logarithmic (or Eulerian) averaged strain increments, identified by the superscript ln. The stresses in Eq. (4) are Cauchy stresses, that is they are defined in the deformed configuration. The determination of the Cauchy stresses in the triaxial stresses is also given in Appendix B.

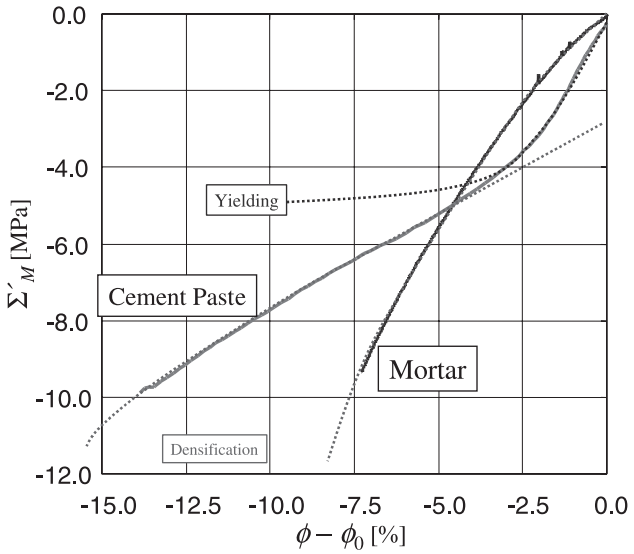

Fig. 3. Results from drained hydrostatic compression tests. The constant pore pressure in these tests is $p = 0.5$ MPa. The dotted lines correspond to the extrapolated individual physical deformation mechanisms discussed.

Based on the partition of the external work rate in Eq. (4), we present the results in the following three types of result plots:

(1) The natural axial strain, $\delta E_{zz}^{\ln} = \ln(L/L_{\mathrm{ref}})$, over the natural volumetric strain, $\delta E_{\mathrm{v}}^{\ln} = \ln(1 + \phi - \phi_{\mathrm{ref}})$, where L_{ref} and ϕ_{ref} are reference values of the sample length and the porosity at the end of the hydrostatic prestressing (consolidation).

(2) The deviatoric stress, $\delta\Sigma_{zz} = \Sigma_{zz} - \Sigma_{rr}$, over the natural deviatoric strain, $\delta E_{zz}^{\ln} - (1/3)\delta E_{\mathrm{v}}^{\ln}$. These results provide insight into the importance of the shear work term in Eq. (4).

(3) The change in mean stress, $\delta\Sigma_{\mathrm{M}} = \Sigma_{\mathrm{M}} - \Sigma_{\mathrm{M}}^{\mathrm{hyd}} = \delta\Sigma_{zz}/3$, over the change in porosity $\delta\phi = \phi - \phi_{\mathrm{ref}}$, where ϕ_{ref} is the porosity at the end of the hydrostatic loading phase. These results provide insight into the volumetric deformation behavior, featuring either contracting ($\mathrm{d}\phi < 0$) or dilating behavior ($\mathrm{d}\phi > 0$). In addition, these results give an evaluation of the volumetric work term in relation (4).

3. Hydrostatic compression tests

3.1. Results

The results from a typical drained hydrostatic compression test on a leached mortar and paste are displayed in Fig. 3 in the form of the mean stress Σ'_{M} versus the change in Lagrangian porosity $\phi - \phi_0$. At low-confinement pressure, the mortar has a higher deformability than the cement paste, but for high confinement, it is the inverse:

- The cement paste follows an s-shaped hardening: after an initial elastic phase, the tangent stiffness decreases first. Then, at higher confinement pressure, the material stiffens (increase of tangent stiffness).
- The mortar stiffens continuously from above, meaning that the tangent stiffness $\mathrm{d}\Sigma_{\mathrm{M}}/\mathrm{d}\phi$ increases continuously in hydrostatic compression.

Fig. 4a and b shows results from a series of hydrostatic loading and unloading tests. They illustrate that the overall stiffening of both materials is irreversible: the slopes of elastic loading–unloading increase for both materials with increasing confinement.

3.2. SEM investigation

SEM micrographs show the expansion of the solid matrix into the pore space. In the case of mortar, the Interfacial Transition Zone (ITZ) is crushed through the confinement.[2]

The deformation behavior under hydrostatic compression can be illustrated with SEM micrographs on compressed specimens (Figs. 6a–c and 9a–b).

[2] Throughout the paper, the main idea of a paragraph is stated in italics to facilitate the reading.

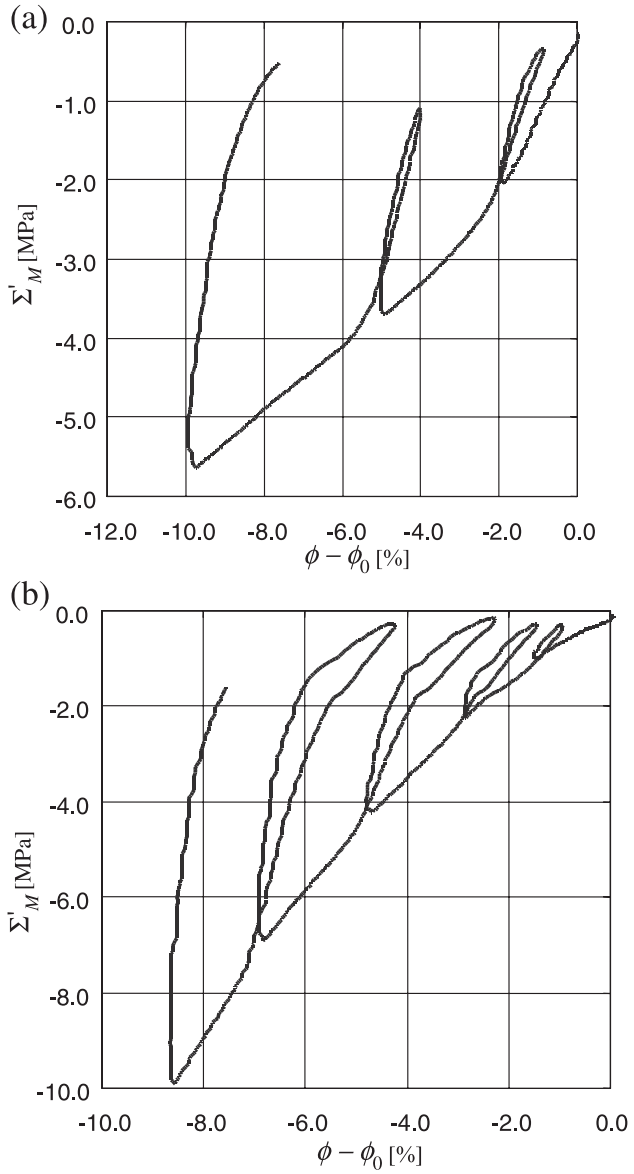

Fig. 4. Hydrostatic compression loading–unloading cycles on (a) cement paste and (b) mortar. The pore pressure is constant at $p = 0.5$ MPa.

Typical SEM image of the highly perforated microstructure of a leached cement-paste matrix before hydrostatic compression are displayed in Fig. 5a–c; Fig. 6a–c displays the same after hydrostatic compression to $\Sigma'_M = -9$ MPa. Before loading, the microstructure of leached pastes is characterized by large pores created by the Portlandite dissolution and a relatively homogeneous microstructure composed of C–S–H that dissolve and reprecipitate at a low *C*/*S* ratio close to 1. The visible pore size range in the leached cement-paste matrix (Fig. 5a–c) varies from 0.1 to 10 μm. The lower value is comparable to the typical pore size of 0.1 μm of macropores in intact cementitious materials at the same *w*/*c* ratio (see for example Refs. [21,22]). The higher value corresponds approximately to the typical size of calcium hydroxide (Portlandite) clusters in intact cementitious materials [22], as displayed in Fig. 7a. The large Portlandite crystals are dissolved first in the course of calcium leaching. During the hydrostatic loading,

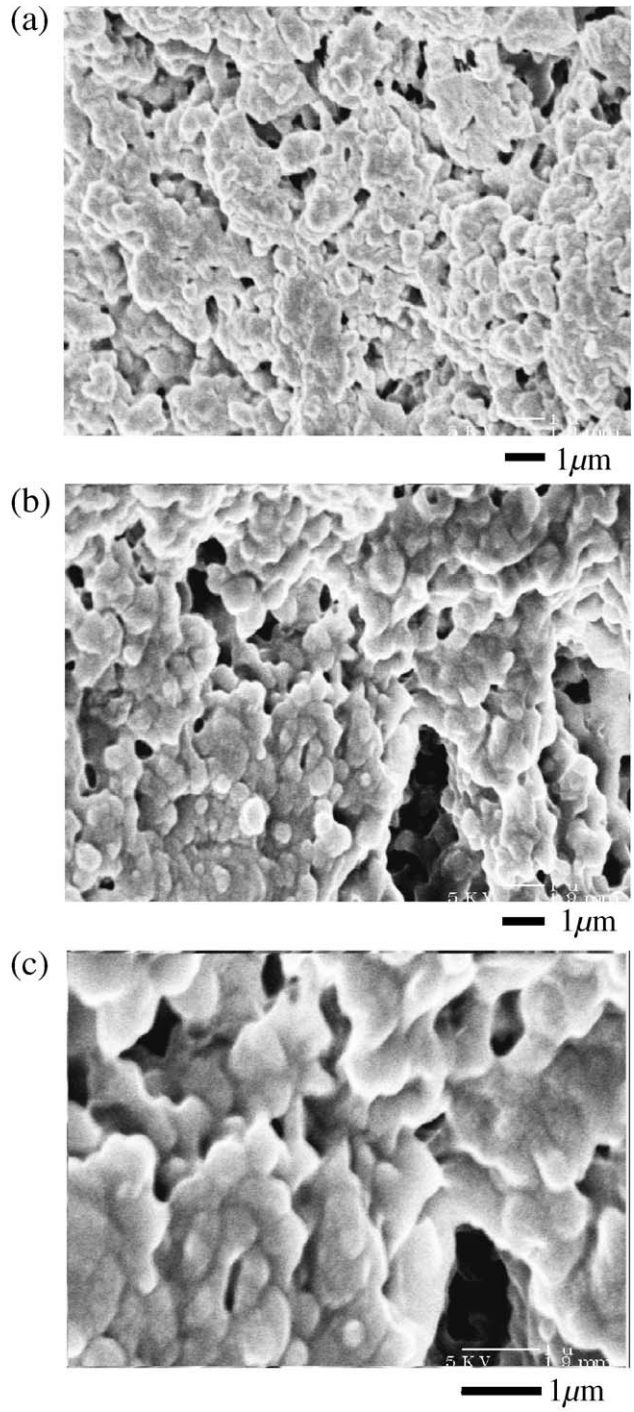

Fig. 5. SEM micrographs of microstructure of leached paste. The characteristic texture of the unleached microstructure, i.e., the clusters of hydration products, has been largely eroded. (a) Uniform washed-out appearance of the leached microstructure, with a large density of new pores in the range of 100 nm. (b and c) Pores in the micrometer range created from the dissolution of large Portlandite crystals.

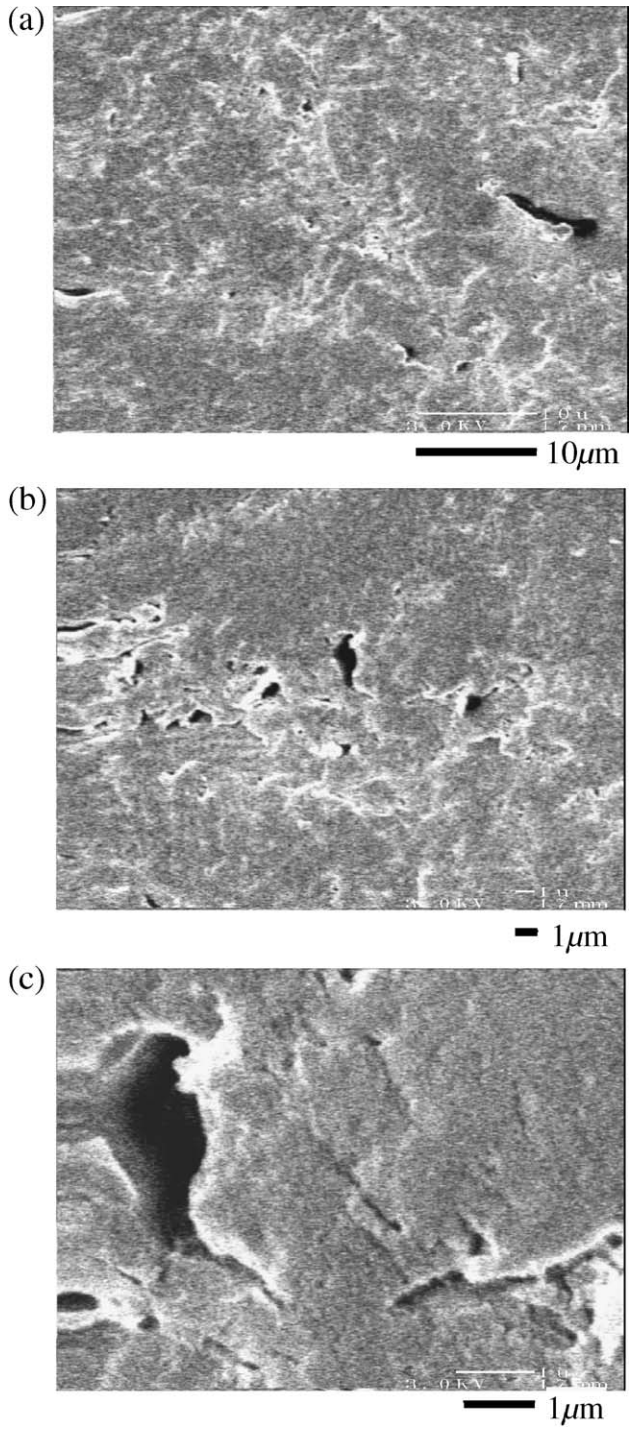

Fig. 6. SEM micrographs of a leached cement paste after hydrostatic compression, $\Sigma'_M = -9$ MPa, $p = 0.5$ MPa. (a) Collapse of large pores, the remnants of the Portlandite dissolution, from an initially rather circular shape into flat pores of elliptical shape. (b) Zones of large localized shear deformation. (c) Expansion of solid into pore space.

the large pore space created by the Portlandite dissolution is reduced. More particularly, it appears from the SEM images that the surrounding solid expanded during loading into the pore space (Fig. 6c), thus reducing the porosity. Some zones show large localized shear deformation, for example in Fig. 6a–b. Moreover, large pores, the remnants of the Portlandite dissolution, may collapse from an initially rather circular shape into flat pores of elliptical shape (Fig. 6a).

In the case of mortars, the deformation of the ITZ creates a different deformation behavior compared with the cement paste. The porosity in the ITZ of leached mortars is particularly high due to the higher Portlandite concentrations in the ITZ of intact mortar [22], as displayed in Fig. 7b. The dissolution of the ITZ-Portlandite leads to the highly porous structure of the ITZ in leached mortar, as displayed by the series of SEM images in Fig. 8 in the vicinity of a sand grain (left part of picture) before hydrostatic loading. While the pore sizes are on the same order of 1–10 μm as in the bulk paste (Fig. 5), the total porosity is much larger in this zone which constitutes the ITZ. This has an effect on the deformation response under hydrostatic compression. Fig. 9a–b shows the grain–matrix interface of a leached mortar after hydrostatic compression to $\Sigma'_M = -9$ MPa. The SEM micrographs show that the micrometer-size porosity in the ITZ vanishes

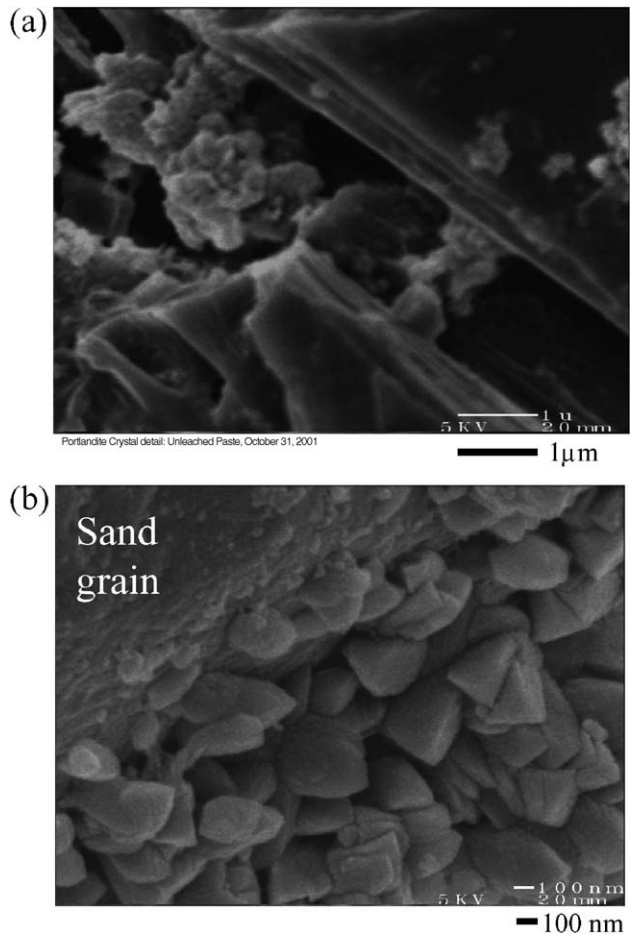

Fig. 7. SEM micrographs of Portlandite appearance in intact cementitious materials. (a) Large Portlandite crystals and clusters in a paste. (b) Higher Portlandite concentration in the ITZ (wall effect).

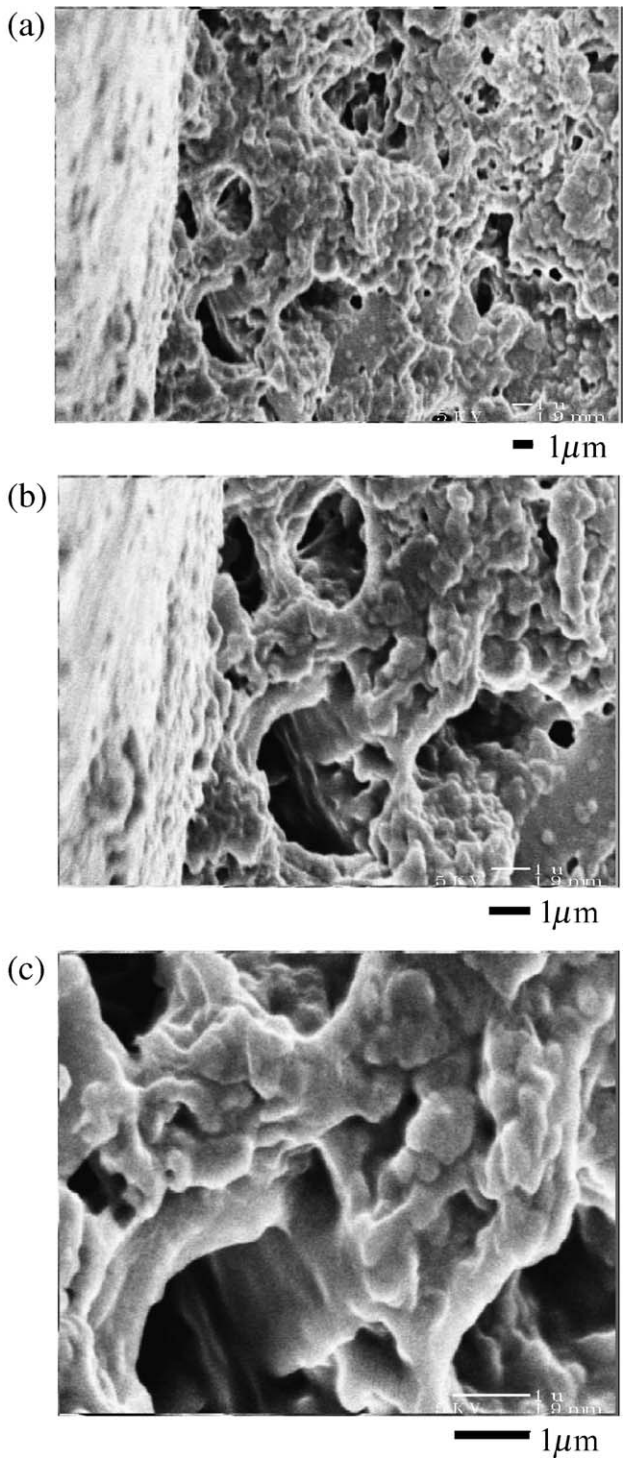

Fig. 8. Sequence of SEM micrographs of ITZ in leached mortar. Images (a–c) show at increasing magnification the grain–paste interface (grain in the left part of graphs).

under stress application (the gaps next to the sand grains are due to the surface polishing). At the same time, the matrix is squeezed into the space between the sand grains, and no shear bands or dramatic changes in the pore morphology are observed.

3.3. Discussion

Two main elements that control the deformation behavior of the leached materials can be extracted from the hydrostatic test results and the SEM micrographs.

(1) *Decalcified C–S–H deform at constant volume into the pore space.* The plastic deformability of the solid of the cement-paste matrix, which is composed, after leaching, mostly of low *C*/*S* C–S–H: the expansion of the solid into the macropores (Fig. 6c) indicates that low *C*/*S* C–S–H at yield deform either at constant volume (incompressible) or under microscopic dilatation, merging in some places into shear bands of concentrated plastic deformation as observed in Fig. 6b. The plastic yield of the solid into the macropores explains the first part of the s-shaped overall contractive hardening behavior of the cement paste occurring at decreasing tangent stiffness (see Fig. 3). Once the solid has filled a large part of the pores, the free yield of the solid material is restrained, leading to the observed stiffening of the material.

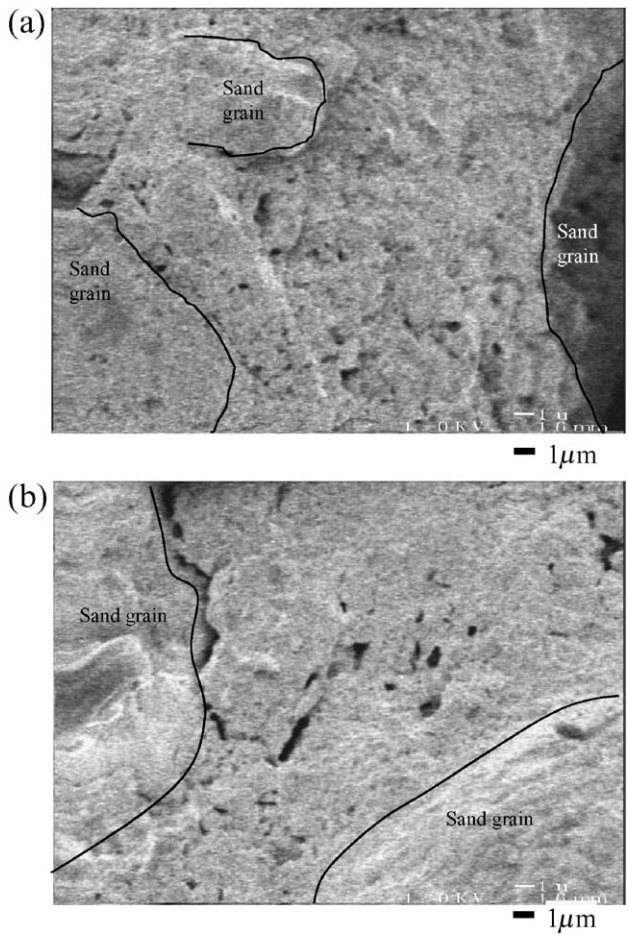

Fig. 9. SEM micrographs of hydrostatically compressed leached mortar, $\Sigma'_M = -9$ MPa, $p = 0.5$ MPa. The marked regions correspond to sand grain locations. Note that some grains are loosened during the polishing process.

(2) *Collapse of macropores leads to geometrical hardening.* The new pore size family generated by leaching of CH clusters, is an order of magnitude larger than typical pore sizes encountered in intact cement-paste materials. In the cement-paste matrix, the large pores offer free expansion space for the plastic deformation of the low *C*/*S* solid. At high confinements, these pores collapse, which contributes to the second part of the s-shaped compaction behavior of the cement paste, associated with a *geometrical hardening* (change in pore morphology). In contrast to the paste, the continuous stiffening of mortar indicates that the mortar's response is dominated by geometrical hardening of the leached ITZ porosity alone. At the given level of hydrostatic compaction, the main change in porosity of the mortar results from the compaction of the ITZ porosity.

4. Deviator loading at increasing confinement

4.1. Results

The confinement level at the beginning of the deviatoric loading has a strong influence on the deformation behavior of leached pastes and mortars. We therefore show results for a low ($\Sigma_M^{hyd} = -1.5$ MPa) and a high ($\Sigma_M^{hyd} = -6.5$ MPa or $\Sigma_M^{hyd} = -7.6$ MPa) confinement level, where Σ_M^{hyd} is the mean stress applied during the initial hydrostatic loading phase. The pore pressure is kept constant at $p = 0.5$ MPa during the tests. Fig. 10 plots the (logarithmic) volume strain δE_v^{ln} in the triaxial test at increasing confinement, driven by the (natural) axial strain, $\delta E_{zz}^{ln} = \ln(L_t/L_{hydro})$. Fig. 11a–b shows the corresponding deviatoric stress development, $\Sigma_{zz} - \Sigma_{rr}$, over the associated (energy-conjugated) strain quantity, $\delta E_{zz}^{ln} - \delta E_v^{ln}/3$; Fig. 12a–b displays the change in mean stress, Σ_M versus the change in Lagrangian porosity ϕ recorded during deviatoric loading. In all deviatoric loading tests at increasing confinement, the same typical picture emerges.

- *While the initial deformational behavior for both materials is similar, at higher strains, the rigid inclusions limit the mortar deformability.* The initial almost linear relation between the axial strain and the volumetric strain (Fig. 10) is independent of the type of material and confinement pressure. This indicates, in accord with the work rate expression (4), that the initial shear deformation of cement pastes and mortars is the same. Since the inclusions are almost rigid, this shear deformation is the one of the cement-paste matrix, including for mortar the ITZ. The lower overall deformability of the mortar due to the presence of rigid inclusions leads to higher deviatoric stresses $\Sigma_{zz} - \Sigma_{rr}$ in the mortar than in the cement paste (Fig. 11a–b).
- *Cement pastes show a stronger contracting behavior. Failure in both materials is associated with zero volumetric deformations.* Cement pastes show a stronger contracting behavior than mortars (higher deformability) (Fig. 12), and

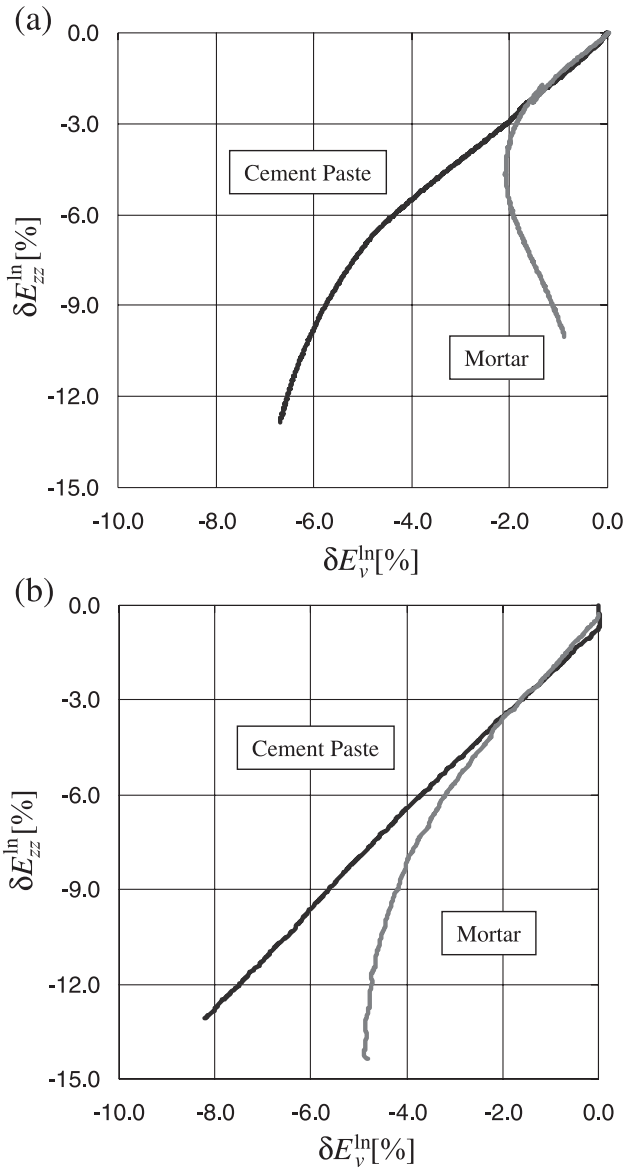

Fig. 10. Axial over volumetric (natural) strain for (a) low confinement, $\Sigma_M^{hyd} = -1.5$ MPa and (b) high confinement, $\Sigma_M^{hyd} = -6.5$ MPa for the paste and $\Sigma_M^{hyd} = -7.6$ MPa for mortar. $p = 0.5$ MPa in all tests.

while cement pastes continue to contract, mortars have an early tendency to develop a dilating behavior ($d\phi > 0$), leading to failure (Fig. 12). The point at which the macroscopic contracting behavior switches into a macroscopic dilating behavior corresponds to the maximum deviatoric stress the materials can support (Fig. 11). Below this point, that is, during contraction, the material hardens continuously. Beyond this point, softening takes place. Hence, a pure shear deformation characterizes this point. The zero volumetric deformation can be associated with what is known as "critical state",[3] at which calcium-leached mate-

[3] The critical state concept was originally developed in Soil Mechanics and characterizes a state of pure shear deformation. See for example Ref. [23].

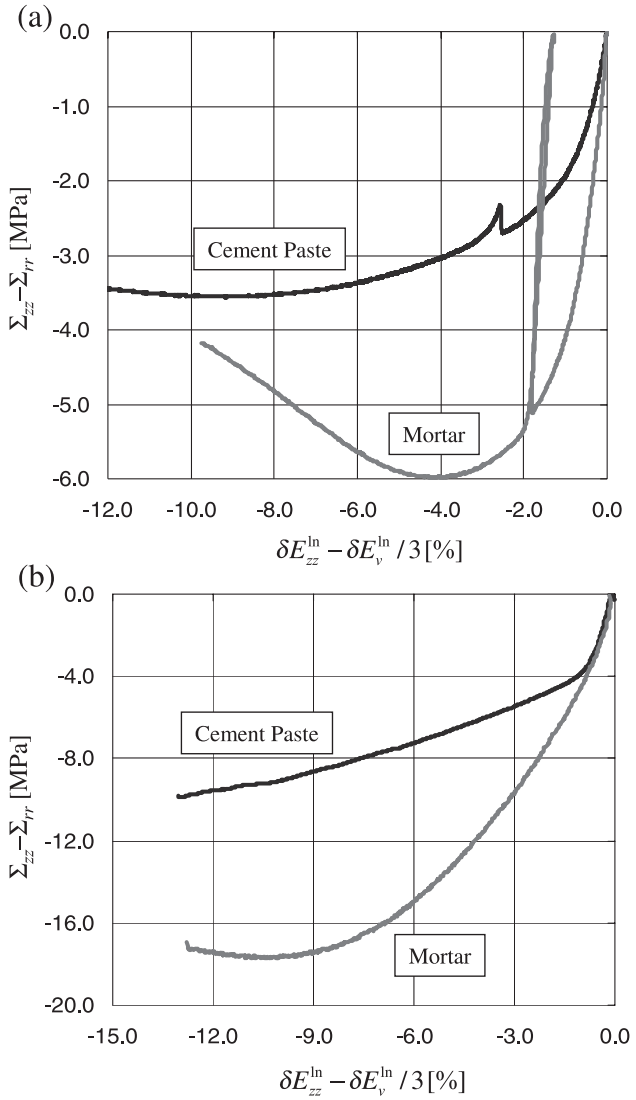

Fig. 11. Deviatoric stress and strain evolution for (a) low confinement, $\Sigma_{\mathrm{M}}^{\mathrm{hyd}}=-1.5$ MPa and (b) high confinement, $\Sigma_{\mathrm{M}}^{\mathrm{hyd}}=-6.5$ MPa for the paste and $\Sigma_{\mathrm{M}}^{\mathrm{hyd}}=-7.6$ MPa for mortar. $p=0.5$ MPa in all tests.

rials lose their capacity to support higher loads. This is consistent with the found shear planes along which the materials fail. Fig. 13 shows a typical failure surface of a leached paste specimen.

4.2. Discussion

The solid material of the paste expands into the void space. Shear band development limits the strength for low confinements. The large compressibility of cement pastes is clearly a consequence of the large plastic deformation the low *C/S* solid can develop in compression and which is even enhanced by deviatoric loading. In fact, for the same confinement level, the overall compaction expressed as the change in porosity in deviatoric loading is larger than in hydrostatic compression (compare Figs. 3 and 12. This supports that the low *C/S* solid expands into the large pore space when subjected to shear deformation, leading to an additional reduction of the overall porosity, in addition to deformation caused by pure hydrostatic compression. Furthermore, the shear deformation of the solid enhances the creation of shear bands in the cement paste, which ultimately exhausts the volume deformability at low confinement, leading to failure. Failure is not achieved for the highly confined cement pastes. The material continues to contract quasi-linearly with the prescribed vertical strain (Fig. 10b). Both the deviatoric stress–strain curve (Fig. 11b) and the mean stress–porosity curve (Fig. 12b) have a distinct yield point, which is associated with the onset of plastic yielding of the solid, and beyond which the

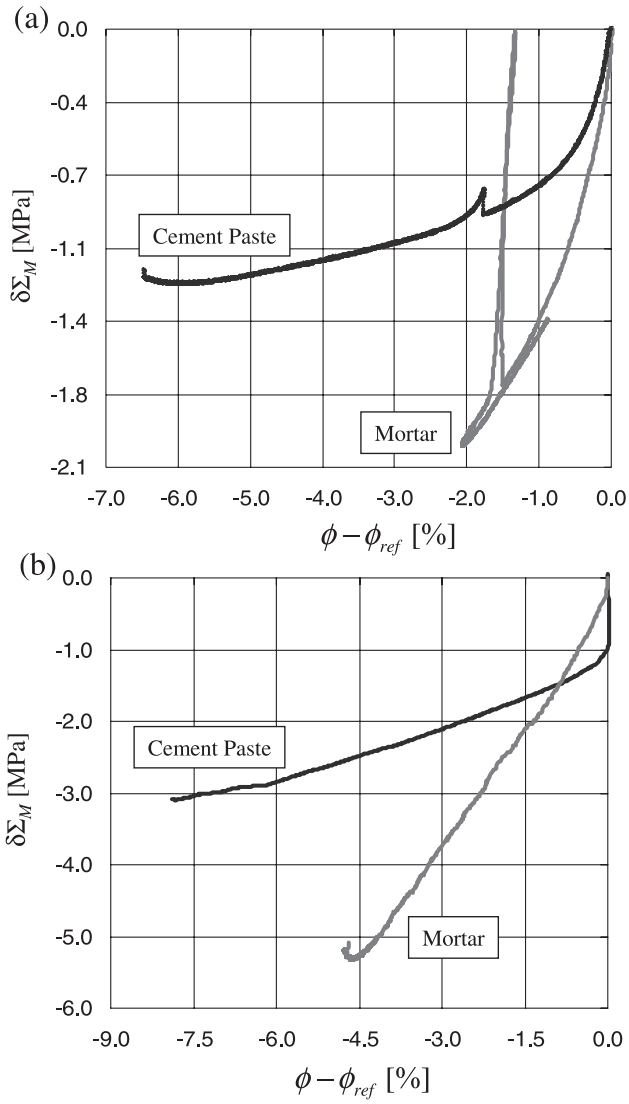

Fig. 12. Change in mean stress and Lagrangian porosity for (a) low confinement, $\Sigma_{\mathrm{M}}^{\mathrm{hyd}}=-1.5$ MPa and (b) high confinement, $\Sigma_{\mathrm{M}}^{\mathrm{hyd}}=-6.5$ MPa for the paste and $\Sigma_{\mathrm{M}}^{\mathrm{hyd}}=-7.6$ MPa for mortar. $p=0.5$ MPa in all tests.

Fig. 13. Typical leached cement-paste specimen fragment after failure on the shear plane.

material exhibits continuous hardening, and this up to large strains of 10% and more.

The ITZ limits the shear deformation capacity of mortars. The early tendency of the mortar to develop a dilating behavior can be attributed to the ITZ. At low confinement, the deviatoric loading generates shear in the ITZ, which favors the coalescence of the ITZ into continuous shear bands between inclusions, leading to failure. The low volume contraction at low confinement (Fig. 12a), appears as a consequence of the shear deformation at constant volume of the solid phase of the matrix, which fills a part of the ITZ porosity, thus geometrically hardening the material. On the other hand, at high confinement, the solid phase first expands into the ITZ porosity, leading to a continuous geometrical hardening of the composite (Fig. 12b), for which—in contrast to the cement paste—no distinct yield point is observed. Once the pores in the ITZ are filled or crushed, it is likely that frictional dilatation developing at the densified matrix–grain interface leads to failure of the mortar. In all cases, the onset of the overall dilating behavior defines the critical state of the material, beyond which material softening occurs. The contracting behavior and the tendency towards a critical state suggest that the yield surface is closed on the hydrostatic axis. The 'critical state' of zero volume change can be associated with the triaxial strength of the material.

5. Deviatoric loading at decreasing confinement

The series of deviatoric loading tests with decreasing confinement is intended to illustrate the effects of a strong initial confinement, as it is relaxed, on the deviatoric deformation behavior. Particularly, the question about the persistence of the stabilizing effect of the hydrostatically induced geometrical hardening is of interest.

5.1. Results

Figs. 14a, 15a, and 16a show the results at the controlled deviator-to-confinement ratio $\gamma = \delta(\Sigma_{zz} - \Sigma_{rr})/\delta\overline{p} = -0.86$. Figs. 14b, 15b, and 16b show the same type of results for the deconfinement ratio $\gamma = -3$. In both cases, the leached paste and mortar have been hydrostatically precompressed to $\Sigma_M^{hyd} \approx -10$ MPa and the pore pressure is kept constant at $p = 0.5$ MPa.

- *Depending on the stress path, dilating or contracting behavior is encountered.* The extent to which the confinement is reduced leads to some important differences in the material behavior. In the δE_{zz}^{ln} vs. δE_v^{ln} plot, a high deconfinement ($\gamma = -0.86$) leads to a dilating behavior (Fig. 14a), while a low deconfinement ($\gamma = -3$) preserves a contracting

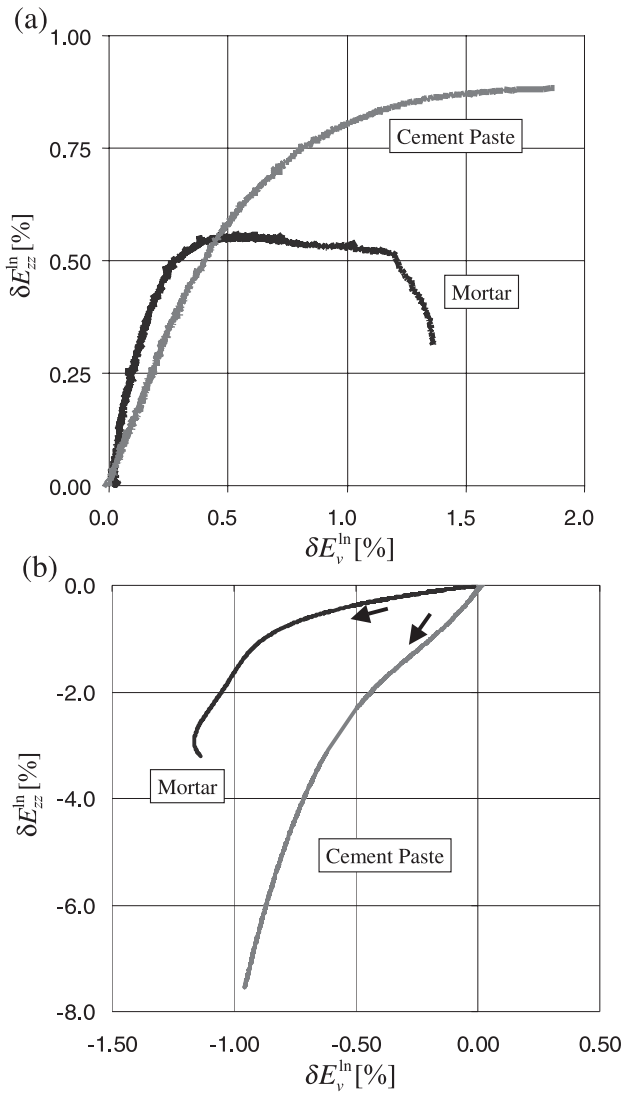

Fig. 14. Change in the axial and logarithmic strains under deviatoric loading at decreasing confinement: (a) $\gamma = -0.86$, (b) $\gamma = -3$. The arrows denote the direction of the test. Note that an initial hydrostatic loading of $\Sigma_M^{hyd} \approx -10$ MPa took place before ($p = 0.5$ MPa).

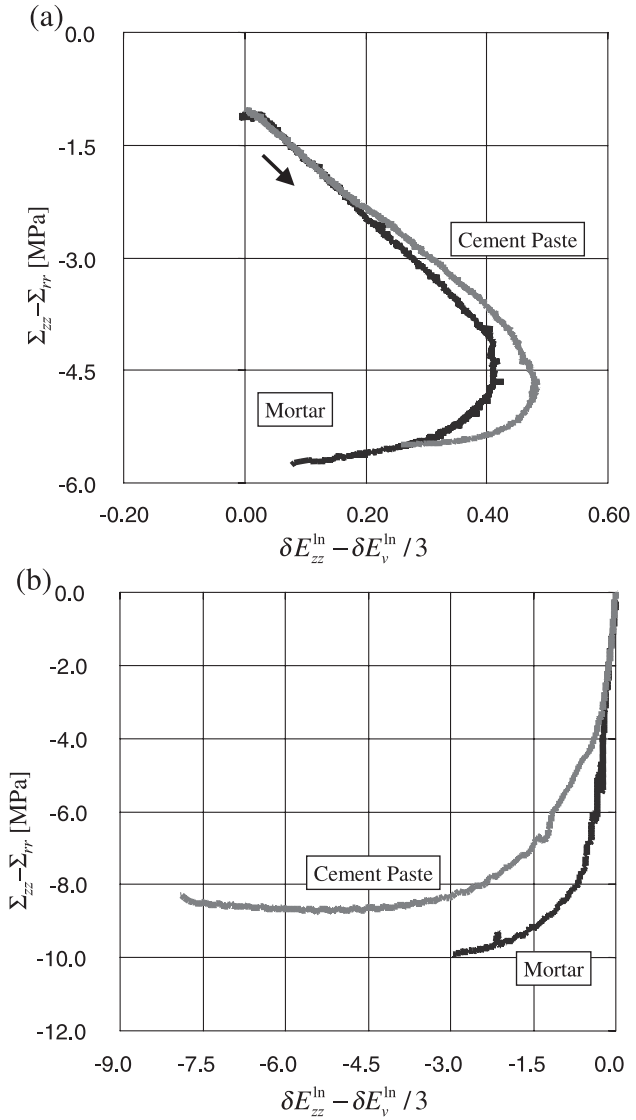

Fig. 15. Evolution of the deviatoric stress vs. natural deviatoric strains: (a) $\gamma=-0.86$, (b) $\gamma=-3$. The arrows denote the direction of the test. Note that an initial hydrostatic loading of $\Sigma_M^{hyd}\approx-10$ MPa took place before ($p=0.5$ MPa).

behavior despite the reduction in confinement (Fig. 14b). For the high deconfinement, after an initial elastic part dominated by the axial deformation, the dilatation becomes dominant in the shear deformation, $\delta E_{zz}^{\ln}-(1/3)\delta E_{v}^{\ln}$. This sensitivity to dilatation is more pronounced for the mortar than for the cement paste. By contrast, at low deconfinement, the overall contraction behavior tends towards a minimum, beyond which dilatation takes place, which is similar to behavior observed in deviatoric loading at increasing confinement.

● *High deconfinement first leads to unloading before softening occurs. Low deconfinement immediately leads to hardening.* The deviatoric response captured in Fig. 15a for high deconfinement, $\gamma=-0.86$, shows a clear yield point at a deviatoric stress of around -4.5 MPa for both cement paste and mortar. Below this point, the incremental work associated with shear deformation $dW_{ext}\propto(\Sigma_{zz}-\Sigma_{rr})(dE_{zz}^{\ln}-dE_{v}^{\ln}/3)<0$ (from Eq. (4)), meaning that this loading phase corresponds effectively to an unloading. Beyond this point, $(\Sigma_{zz}-\Sigma_{rr})(dE_{zz}^{\ln}-dE_{v}^{\ln}/3)$ increases (Fig. 15a), leading to some limited hardening, given that $dE_{zz}^{\ln}-dE_{v}^{\ln}/3\rightarrow 0$. By contrast, at low deconfinement $\gamma=-3$, the incremental shear work is positive from above, leading to the elastoplastic hardening behavior shown in Fig. 15b.

● *In high-deconfinement tests, the materials dilate, while in low-deconfinement tests, the materials contract towards the critical state.* The high deconfinement ($\gamma=-0.86$) provokes a progressive dilatation of the material (Fig. 16a), for which the volumetric work $\Sigma_M' d\phi<0$. By contrast, $\Sigma_M' d\phi>0$ at low deconfinement ($\gamma=-3$), for which the

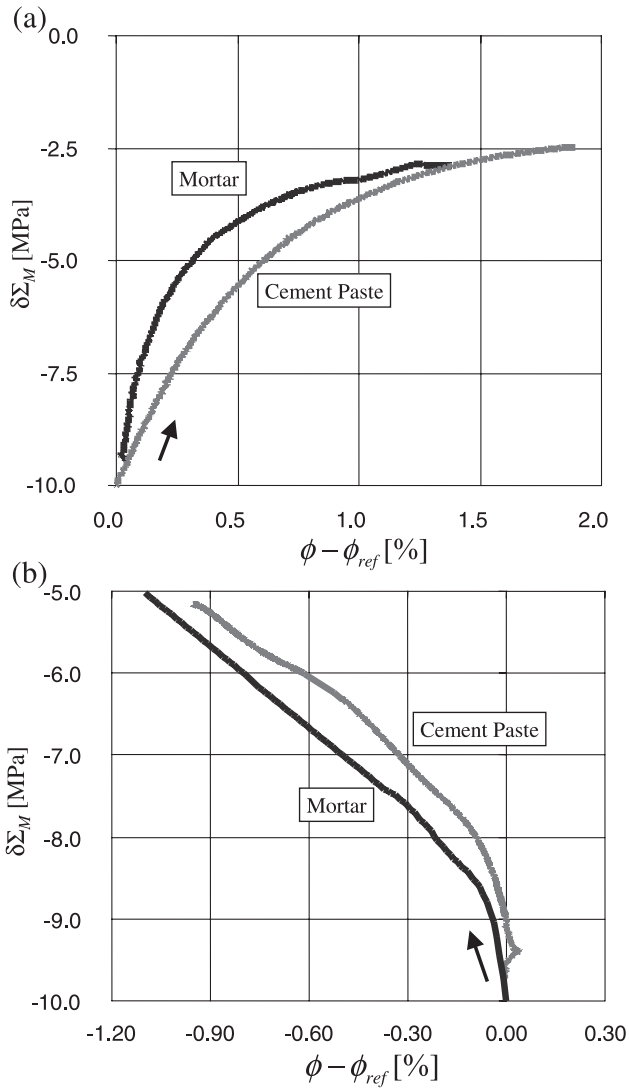

Fig. 16. Evolution of the effective mean stress vs. Lagrangian porosity change: (a) $\gamma=-0.86$, (b) $\gamma=-3$. The arrows denote the direction of the test. Note that an initial hydrostatic loading of $\Sigma_M^{hyd}\approx-10$ MPa took place before ($p=0.5$ MPa).

material contracts almost linearly as the confinement is reduced (Fig. 16b).

5.2. Discussion

Shear bands lead to failure. In both loading cases, an increasing deviatoric loading induces shear deformations in the highly compacted matrix. The large dilatation that occurs in the high-deconfinement test indicates that the solid in this loading case has little space left to expand in the free pore space. Indeed, this space has been crushed during the initial hydrostatic loading to $\Sigma_M^{hyd} \approx -10$ MPa. In the cement paste, the solid deforms, eventually at constant volume, into the shear bands, leading to the failure of the material along shear plans. The failure mechanism is similar for the mortar: as the cement-paste matrix deforms, it activates the compacted ITZ, leading to shear failure along shear bands connecting almost rigid inclusions.

In low deconfinement, the shear deformation dominates the total deformation. At low deconfinement, the initial elastic dilatation of the material generates sufficient pore space for the solid phase to deform, without creation of shear bands in the cement-paste matrix. Given that the porosity decreases overall (Fig. 16b), the volume required by the shear deformation of the solid is larger than the porosity generated by elastic dilatation. This leads to an overall compaction and to the pronounced plastic behavior of both cement paste and mortar shown in Fig. 15b. Once the volume deformability is exhausted, the materials fail in a similar fashion as specimens in deviatoric loading at increasing confinement.

In high-deconfinement tests, softening is observed, leading to final stress states on the critical state line. In high-deconfinement tests, after reaching the maximum deviatoric stress (Fig. 15a) a strong softening is observed, associated with dilating deformation. This is not depicted on Fig. 15a because the test control cannot keep the stress path on the $\gamma = -0.86$ trajectory, precisely because of the strong softening behavior. The stable stress state after softening takes place is on the critical state line and associated with zero volumetric deformation. The fact that dilating softening occurs in a high-deconfinement test at increasing deviatoric load suggests that the yield surface is not only closed on the hydrostatic axis in compression but also closed on the tension side of the hydrostatic axis, with the critical state line dividing zones of dilating and contracting behavior.

6. Triaxial strength domain and effective stress concept

6.1. Results

In the hydrostatic tests, no failure of the specimen takes place. By contrast, in the deviator loading tests at increasing confinement, ductile failure of cement pastes occurs on a shear plane once the material has exhausted its volumetric deformability ('critical' state). The angle of this plane with the vertical axis increases with the confinement. In turn, mortar specimens, in a deviator loading test at increasing confinement, fail in a relatively large bulk zone. Both materials, after calcium leaching, are frictional materials increasing in ultimate strength with mean stress.

- The drained failure points of cement paste and mortar shown in Fig. 16a–b align on a straight line in the $|\Sigma_{zz} - \Sigma_{rr}| \times \Sigma_M$ plane. The maximum strength coincides with zero volume deformation. The straight lines in Fig. 16, therefore, describe the critical states of the leached cementitious materials. The critical state line has been reported in Ref. [16] for cement pastes,[4] and for mortars in Ref. [24], in the form of the Drucker–Prager failure surface parameters, friction angle α, and cohesion c. For purpose of completeness, Table 2 summarizes the true drained Drucker–Prager failure surface parameters determined from the Cauchy stresses for unleached and leached cement pastes and mortars:

$$F(\Sigma_{ij}) = \sqrt{J_2} + \alpha\Sigma_M - c \leq 0 \tag{5}$$

where $\sqrt{J_2} = \sqrt{(1/2)S_{ij}S_{ij}} = \sqrt{1/3} \times |\Sigma_{rr} - \Sigma_{zz}|$ is the second invariant of stress deviator $S_{ij} = \Sigma_{ij} - \Sigma_M\delta_{ij}$ (δ_{ij} is the Kronecker Delta) in the triaxial test.

- Fig. 16b shows the results of the undrained tests on the calcium-depleted mortars. For low-confinement pressures, $\Sigma'_M \geq -2$ MPa, the mortars show some frictional behavior. For higher confinements, the maximum deviator stress remains constant. The almost no friction behavior under drained conditions has been reported and analyzed in Ref. [16] for cement pastes. This finding, which is a consequence of the pore-pressure buildup under undrained conditions, is confirmed here for mortars. It should be noted that the frictional behavior at radial pressures below 2 MPa may well be due to entrapped air in the mortar, leading to a lack of saturation in the beginning of a test. Indeed, the saturation curve for a mortar shows that a complete saturation was reached at about 1.6 MPa.

- The strength of the calcium-depleted materials at decreasing confinement also complies with the Drucker–Prager criterion (Eq. (5)). For the high-deconfinement test ($\gamma = -0.86$), Eq. (5) describes the residual strength after softening, and for the low-deconfinement test ($\gamma = -3$), the maximum strength.

Results from drained tests at different pore-pressure levels are shown in Fig. 18. The pore pressure ranges from $p = 0$ to $p = 9$ MPa. Fig. 18 shows three examples of such test results for $p = 3$, 6, and 9 MPa. Correcting the mean stress Σ_M at failure by the applied pore pressure, that is $\Sigma'_M = \Sigma_M + p$, the obtained strength values in the $|\Sigma_{zz} - \Sigma_{rr}| \times \Sigma'_M$ plane align on the same straight line of the drained test carried out at

[4] Note that in Ref. [16], the stress quantities were reported in the initial configuration, and not in the deformed.

$p=0$ (i.e., Fig. 17b). In terms of the Drucker–Prager yield surface, we have:

$$F(\Sigma_{ij}) = \sqrt{J_2} + \alpha(\Sigma_M + \beta p) - c \leq 0 \quad (6)$$

where β is the Coussy coefficient [20]. The obtained results displayed in Fig. 18 provide conclusive evidence that $\beta=1$ for calcium-depleted cement-paste materials. This phenomenon is referred to as effective stress concept and applies here at failure.

During the experimental investigation, different pore pressures were used to check whether the effective stress concept applies also to the deformation behavior. Fig. 19a displays two typical mean stress–porosity curves of a drained triaxial compression test on cement paste, one carried out at a fluid pressure of $p=0$ MPa, the other at a fluid pressure of

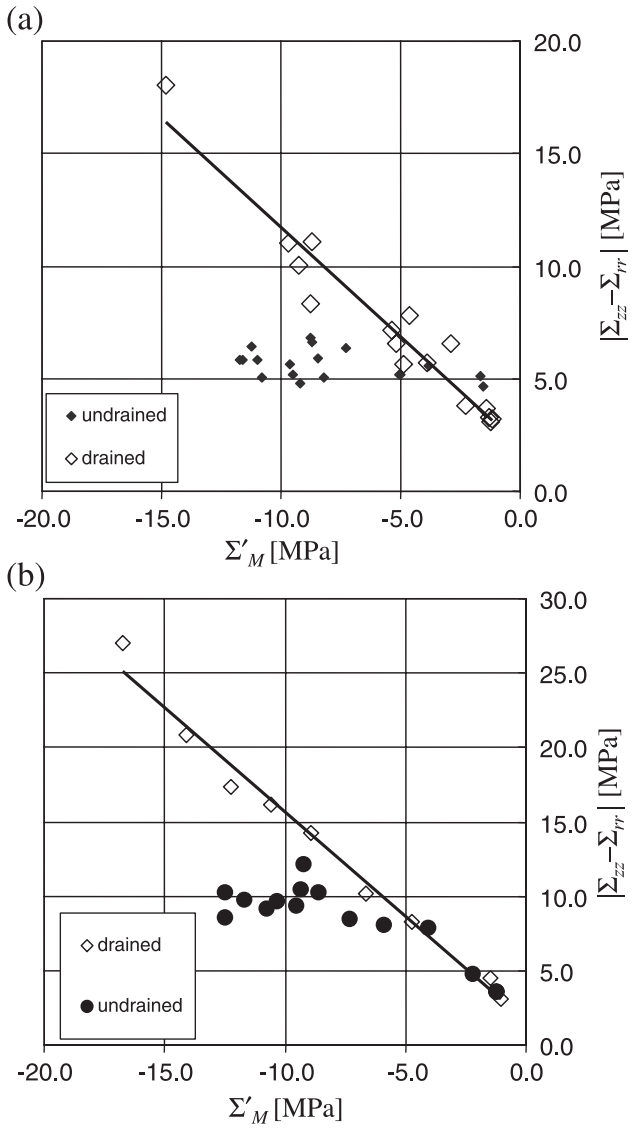

Fig. 17. Critical state line for calcium leached materials: (a) cement paste, (b) mortar.

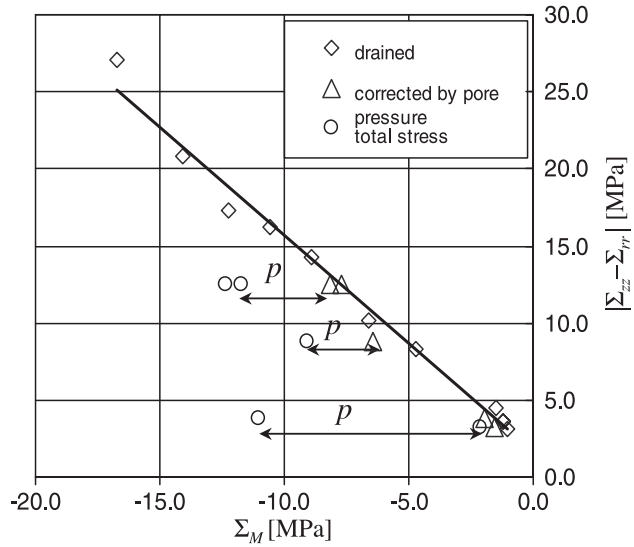

Fig. 18. Drained triaxial strength tests on calcium-depleted mortars with different constant pore pressures: measured total stresses and pore pressure corrections.

$p=6$ MPa, for which the mean stress was corrected following the effective stress concept, $\Sigma'_M = \Sigma_M + p$. The good agreement between the two tests shows that the effective stress concept is valid throughout the loading process. The same is true for the leached mortar as Fig. 19b shows with a comparison of a test at $p=1$ MPa and $p=5$ MPa.

6.2. Discussion

6.2.1. Drained strength

From the drained tests on leached pastes and mortars, we note that the degradation effect is specifically strong on the cohesion c (Table 2). Both the mortar and the cement paste lose almost 90% of their initial cohesion, although the porosities are very different in both materials (see Table 2). This indicates that the changed C–S–H matrix properties are more likely the source for this chemical decohesion rather than the change in porosity, which is to the largest part due to Portlandite dissolution. Mortars have a lower cohesion than the paste which can be attributed to the influence of the ITZ.

By contrast, the degradation of the friction coefficient α is more pronounced for the cement paste which loses 32% of its initial friction coefficient, while it is only 21% for the mortar. This suggests that the influence of the ITZ on the friction coefficient of leached mortars is not as detrimental as the mere increase in porosity in these zones might suggest. The generally higher friction coefficient for mortar that is observed for both the leached and unleached materials is due to the advantageous presence of the aggregates. The ITZ is compressed under the increasing confinement and deactivated (crushing of the ITZ in high confinement as shown in the SEM images in Fig. 9a–b). The relatively larger difference in frictional capacity for

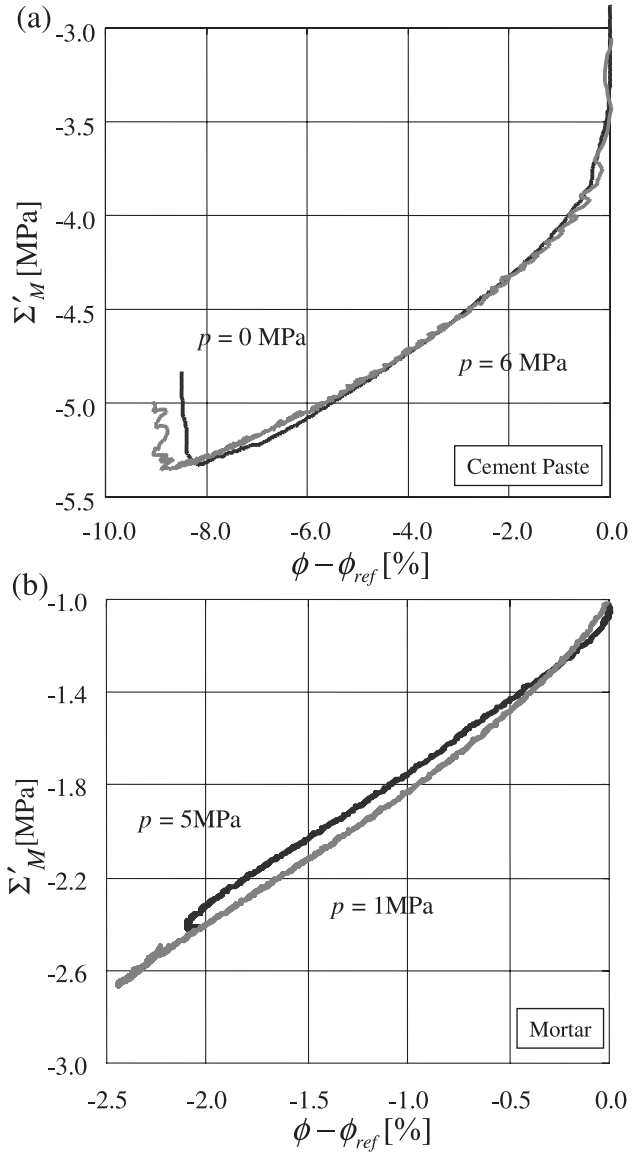

Fig. 19. Effective mean stress $\Sigma' = \Sigma + p$ over porosity change plot for different pore pressures: (a) leached paste; (b) leached mortar.

the leached materials ($\alpha_{paste}/\alpha_{mortar} = 0.69$ for leached and $\alpha_{paste}/\alpha_{mortar} = 0.8$ for unleached materials) shows that this is even more true for the leached materials in which the ITZ is particularly porous.

6.2.2. Effective stress concept and undrained strength

The drained tests with varying pore pressures show that the effective stress concept applies at failure and during the entire loading process. The level of pore pressure, p, determines how much of the applied mean stress is effectively acting on the material. It is known from poromechanics theory [20] that the validity of the effective stress concept indicates the incompressibility of the solid phase, that is,

$$V_s \equiv V_{s0} : \frac{V}{V_0} = 1 + \phi - \phi_0 \qquad (7)$$

Furthermore, given the low elastic strength limit of the materials and consistent with the SEM images in Fig. 6a–c, it is likely that the validity of the effective stress concept is a consequence of the plastic incompressibility of the solid phase in the leached materials.

Finally, the validity of the effective stress concept offers an explanation for the undrained results on the leached paste and mortar, displayed in Fig. 18. The constant undrained deviatoric strength suggests that the pore pressure, p, in undrained tests, rises with the externally applied mean stress Σ_M such that the effective mean stress $\Sigma'_M = \Sigma_M + p = -1.5$ MPa at all times.

7. Conclusions

Asymptotic calcium leaching of cementitious materials produces a new material, composed of a matrix phase (solid + occluded nanoporosity) and porosity. In contrast to intact cement-based material systems, the matrix phase is composed of C–S–H having a low *C/S* ratio close to 1, and the porosity by a new pore size family in the micrometer range, generated by the dissolution of CH clusters. It is suggested that these two phenomena have well-distinct effects on the mechanical behavior of calcium-leached materials.

- The large plastic deformations of the paste show that the low *C/S* C–S–H matrix is highly plastically deformable. This is consistent with the microstructure of low *C/S* ratio C–S–H, characterized by a high polymerization (long SiO_2 chains) and octahedral sheets that are either empty (CaO dissolved), or that contain some iron or aluminum [3,25]. By contrast, in intact cementitious materials, the presence of Portlandite crystals and the characteristics of high *C/S* ratio C–S–H with full octahedral sheets and shorter SiO_2 block such large plastic sliding.
- Decalcifying the C–S–H to low *C/S* ratios goes along with a reduction of the cohesion of the cementitious materials (Table 2). While low *C/S* C–S–H are able to undergo large plastic deformations, at the same time their cohesion is reduced. Our macroscopic results confirm that the cohesion of C–S–H is correlated to the *C/S* ratio, which was found by microstructural modeling of C–S–H properties by other authors [2,26]. Reducing the *C/S* ratio of the C–S–H empties the interlayer void space of the C–S–H, affects their electronic charge, and therefore reduces the cohesion. Given this microstructure, it is reasonable to suggest that the solid composed of low *C/S* ratio C–S–H is a pure cohesive incompressible material.
- The validity of the effective stress concept at failure provides evidence that the solid phase is a pure cohesive material [27]. The validity of the effective stress concept during the entire loading process indicates that the solid is incompressible [20]. The high compaction capacity of calcium-leached materials, then, appears as a consequence of the shear deformation of the pure cohesive heterogeneous solid, which expands into the macroporosity, in order to

preserve its volume. The large pores created by the dissolution of CH clusters provide expansion space for the incompressible plastically deformable solid during deviator loading. Once this porosity is filled, further volume contraction is restrained, which leads to generation of shear bands and macroscopic dilation, which ultimately governs the failure of the cement paste.

- In mortars, a competition between plastic material behavior and porosity-controlled structural deformation takes place. In hydrostatic compression, the mortar's response is governed by geometrical hardening of the ITZ, which crushes the large pores in the ITZ. As shear deformation increases, in compression, the intrinsic plastic deformation properties of the paste dominate first, leading to a pronounced deviator hardening as the solid is squeezed into the pore space. With increasing deviator stress, at low confinements, the incompletely filled ITZ porosity merges into shear bands through the cement paste along which the material fails. At high confinement, a saturation of the porosity by the solid phase exhausts the volume contraction capacity of the material. Additional shear deformation of the solid triggers frictional dilation mechanisms at the densified matrix–grain interface that lead to the observed bulk failure of calcium-leached mortars.
- The observed macroscopic deformation behavior appeals to the adaption of a modified Cam–Clay model [23] for leached cementitious materials. In the stress space, it incorporates the critical state that separates a contracting from a dilating domain. In addition, the hardening is governed by the change in porosity which very much reflects leached cementitious materials. The yield surface, which is displayed in Fig. 20, reads:

$$2f = \frac{3J_2}{m^2} + [\Sigma_M + p + (p_c - p_t)]^2 - (p_c + p_t)^2 \le 0 \qquad (8)$$

where $2p_c$ and $2p_t$ are the closing pressures of the ellipse on the hydrostatic axis. m is close to a constant, the slope of the critical state line that was described in the strength investigation by a Drucker–Prager. More precisely, as the maximum strength coincides with the critical state, the Drucker–Prager line and the critical state line are identical, and m can be determined. The critical state is defined for (see, e.g., Ref. [20]):

$$f = 0: \ \frac{\partial f}{\partial \Sigma'_M} = 0 \Rightarrow \Sigma'_{M,crit} = p_t - p_c \qquad (9)$$

Substituting Eq. (9) in Eq. (8), a comparison with Eq. (6) yields

$$m = \sqrt{3}\alpha; \ p_t = c\frac{\sqrt{3}}{2m} \qquad (10)$$

Finally, the consolidation pressure $p_c(\phi) = -(1/2)(\Sigma_M + p)$ is determined from the hydrostatic compression test displayed in Fig. 3. The description of the macroscopic poroplastic deformation behavior of leached cementitious materials in compression is then complete.

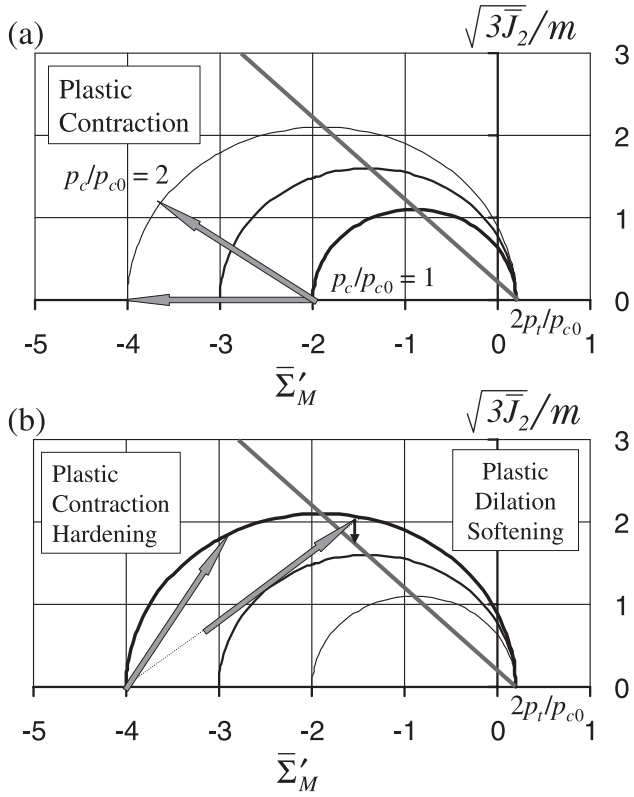

Fig. 20. Cam–Clay model for leached cementitious materials in the stress deviator—effective mean stress half-plane normalized by the initial consolidation pressure $\sqrt{\bar{J}_2} = \sqrt{J_2}/p_{c0}$; $\bar{\Sigma}'_M = (\Sigma_M + p)/p_{c0}$: (a) yield criterion with hydrostatic compression and deviator loading at increasing confinement; (b) yield criterion with deviator loading at decreasing confinement.

Acknowledgements

This research was performed as part of Grant No. DE-FG03-99SF21891/A000 of the US Department of Energy (DOE) to MIT. The authors gratefully acknowledge the support of this work by the Nuclear Energy Research Initiative Program of DOE and the collaboration with the Commissariat à l'Energie Atomique (CEA, Saclay, France), through Dr. Jérôme Sercombe. The research also benefitted from fruitful exchanges with Prof. Luc Dormieux, ENPC, Paris.

Appendix A. Determination of the loading rate to ensure drained conditions

An important parameter in the triaxial tests is the loading velocity. In order to have a truly drained test,

Table 4
Time to failure necessary according to the consolidation theory for a drained test

Specimen	Time to failure
Undegraded	10.6 days
Degraded	4.2 h

the fluid pressure has to remain constant throughout the specimen. This implies that a certain loading rate must not be exceeded which allows the specimen to equilibrate the pore pressure. In a preliminary test on leached and unleached pastes, the necessary total testing time was determined following the procedure suggested by Bishop and Henkel [28], which is based on the consolidation theory by Terzaghi [29]. In hydrostatic compression, a pressure p^0 was applied, and the subsequent volume change was measured over time. From the recorded curve, volume change over square root of time, the time for 100% consolidation is determined along with the consolidation coefficient c_v, which takes into account the drainage conditions (i.e., drainage on one side through the porous stone). Then following consolidation theory, a time for failure t_f is determined which needs to be respected in the tests in order to obtain drained test results. Table 4 gives the t_f values for the degraded and undegraded paste specimens. From the value for the degraded specimen, we deduce a loading strain rate of $|\dot{E}_{zz}| = 5 \times 10^{-6}\ \mathrm{s}^{-1}$, which is kept constant throughout the test series. We assume that the drainage in mortars is at least as good as in cement paste so that the same loading rate is being used. From the time to failure for undegraded materials, it appears that a drained test for these materials is difficult to realize. During tests of a duration of several days or weeks, creep effects would become important, which may suggest that there is some connection between creep and drainage conditions for the undegraded saturated pastes. The triaxial strength tests on undegraded specimens were run at the same strain rate as the degraded ones, which means that they cannot be considered completely drained.

Appendix B. Conjugated Cauchy stress and logarithmic strain measurements

The strains in the triaxial tests are evaluated with respect to the current deformed configuration, leading to Euler strains, natural strains, or logarithmic strains,[5] identified by the superscript "ln". In particular, the volumetric strain is evaluated from:

$$E_v^{\ln} = \int_{V_0}^{V} \frac{\mathrm{d}V}{V} = \ln \frac{V}{V_0} \tag{11}$$

The axial strain of a cylindrical specimen reads:

$$E_{zz}^{\ln} = \int_{L_0}^{L} \frac{\mathrm{d}L}{L} = \ln \frac{L}{L_0} \tag{12}$$

The conjugated stresses-to-strain measurements can be determined from the external work rate which reads:

$$\frac{\mathrm{d}W_{\mathrm{ext}}}{\mathrm{d}t} = \int_V \Sigma_{ij} D_{ij} \mathrm{d}V + p \frac{\mathrm{d}V_f}{\mathrm{d}t} \tag{13}$$

where Σ_{ij} is the Cauchy stress tensor, D_{ij} is the tensor of Euler strain rates, the integration of which leads to logarithmic strains, and p is the fluid pressure. Introducing the strain definitions in Eqs. (11) and (12) and assuming a cylindrical stress state characterized by a radial stress Σ_{rr} equal to the hoop stress $\Sigma_{\theta\theta}$ and an axial stress Σ_{zz}, Eq. (13) becomes:

$$\frac{\mathrm{d}W_{\mathrm{ext}}}{\mathrm{d}t} = 2\Sigma_{rr} \frac{\mathrm{d}E_{rr}^{\ln}}{\mathrm{d}t} V + \Sigma_{zz} \frac{\mathrm{d}E_{zz}^{\ln}}{\mathrm{d}t} V + p \frac{\mathrm{d}V_f}{\mathrm{d}t} \tag{14}$$

or equivalently, using Eq. (2) and dividing the work rate in a volumetric and a deviatoric part:

$$\frac{\mathrm{d}W_{\mathrm{ext}}}{\mathrm{d}t} = (\Sigma_M + p) \frac{\mathrm{d}\phi}{\mathrm{d}t} V_0 + (\Sigma_{zz} - \Sigma_{rr}) \left(\frac{\mathrm{d}E_{zz}^{\ln}}{\mathrm{d}t} - \frac{1}{3} \frac{\mathrm{d}E_v^{\ln}}{\mathrm{d}t} \right) V \tag{15}$$

which is relation (4). The first term represents the work rate provided by the effective stress $\Sigma'_M = \Sigma_M + p$ to the solid phase of the porous material, according Terzaghi's effective stress concept [29]. In fact, Terzaghi's assumption in terms of externally supplied work reads:

$$\Sigma_M \frac{\mathrm{d}V}{\mathrm{d}t} + p \frac{\mathrm{d}V_f}{\mathrm{d}t} \simeq (\Sigma_m + p) \frac{\mathrm{d}\phi}{\mathrm{d}t} V_0$$

which holds strictly for an incompressible solid, for which $\mathrm{d}V_f = \mathrm{d}(V - V_s) = \mathrm{d}V$.

The Cauchy stress Σ_{ij} is defined in the deformed configuration of the porous medium. To calculate the radial and axial stresses, Σ_{rr} and Σ_{zz}, during the test, the deformed section of the cylindrical specimen needs to be determined. Two cases are distinguished:

(1) Under hydrostatic loading, for which $\Sigma_{zz} = \Sigma_{rr} = \Sigma_{\theta\theta}$, the cylindrical shape of the specimen is preserved. The ratio between current and initial volume reads:

$$\frac{V}{V_0} = \left(\frac{R}{R_0} \right)^2 \frac{L}{L_0} \tag{16}$$

[5] In a one-dimensional setting, natural strains are introduced via the integral of $\mathrm{d}l/l$ considering the length change $\mathrm{d}l$ with respect to the current length l. The three-dimensional extension of this concept is due to Hencky [30].

where R and L are the current radius and length, respectively, while R_0 and L_0 are the corresponding values in the initial configuration. To determine the radius R for stress evaluation purposes only, we assume that the change in solid volume is negligible compared to the porosity change in Eq. (3), that is:

$$\frac{V}{V_0} \simeq 1 + \phi - \phi_0 \tag{17}$$

Using Eq. (17) in Eq. (16), the current radius is determined from the porosity measurements and the length change measurement:

$$\frac{R}{R_0} = \sqrt{\frac{L_0}{L}(1 - \phi + \phi_0)} \tag{18}$$

where ϕ_0 is the porosity in the initial configuration. With the updated radius at hand, the vertical stress is readily computed from the recorded vertical force F, that is

$$\Sigma_{zz} = \frac{F}{\pi R^2} \simeq \frac{FL}{\pi R_0^2 L_0 (1 + \phi - \phi_0)} \tag{19}$$

(2) Following hydrostatic loading, a deviatoric loading is applied. In this deviatoric loading, the cylindrical shape of the specimens is not preserved. Instead, the deformed longitudinal shape is observed to be parabolic. In this case, the radius becomes a quadratic function of the vertical coordinate. We note R_{ref}, L_{ref}, and ϕ_{ref}, the radius, length, and porosity at the onset of the deviatoric loading. The maximum radius in the center of the specimen reads:

$$\frac{R_{\max}}{R_{\mathrm{top}}} = \frac{1}{4}\left(\sqrt{30\frac{V}{V_{\mathrm{ref}}} \times \frac{L_{\mathrm{ref}}}{L} \times \left(\frac{R_{\mathrm{ref}}}{R_{\mathrm{top}}}\right)^2 - 5} - 1\right) \tag{20}$$

where R_{top} is the radius at the top of the specimen. This radius is assumed not to change during the deviatoric loading. The ratio between current and reference volume is evaluated, using Eq. (17):

$$\frac{V}{V_{\mathrm{ref}}} = 1 + \frac{\phi - \phi_{\mathrm{ref}}}{1 + \phi_{\mathrm{ref}} - \phi_0};\ \frac{R_{\mathrm{ref}}}{R_{\mathrm{top}}} = 1 \tag{21}$$

Combining Eqs. (20) and (21) yields:

$$\frac{R_{\mathrm{t,max}}}{R_{\mathrm{ref}}} = \frac{1}{4}\left(\sqrt{30\left(\frac{1 + \phi - \phi_0}{1 + \phi_{\mathrm{ref}} - \phi_0}\right) \times \frac{L_{\mathrm{ref}}}{L} - 5} - 1\right) \tag{22}$$

The magnitude of the vertical Cauchy stress in the specimen center is then calculated from the vertical load applied during the deviatoric loading

$$\delta\Sigma_{zz} = \Sigma_{zz} - \Sigma_{zz,\mathrm{ref}} = \Sigma_{zz} - \Sigma_{rr} = \frac{\delta F_z}{\pi R_{\mathrm{t,max}}^2} \tag{23}$$

with $\Sigma_{zz,\mathrm{ref}} = \Sigma_{rr} = \Sigma_{\theta\theta}$, the mean stress at the end of a prior hydrostatic loading ($\Sigma_{rr} = \Sigma_{\theta\theta}$ held constant during deviator loading). "δ" indicates the change in a parameter after the hydrostatic loading phase is concluded.

Note clearly that relation (17) is only used for the evaluation of the Cauchy stresses from the deformed geometry.

References

[1] U.R. Berner, Modelling the incongruent dissolution of hydrated cement minerals, Radiochimica Acta 44–45 (1988) 387–393.

[2] P. Faucon, A. Delagrave, J. Petit, C. Richet, J. Marchand, H. Zanni, Aluminum incorporation in calcium silicate hydrate (C–S–H) depending on their Ca/Si ratio, Journal of Physical Chemistry, B 103 (1999) 7796–7802.

[3] C. Porteneuve, Caractérisation des Bétons par Résonance Magnétique Nucléaire: Application à l'Etude de l'Altération par l'Eau, PhD dissertation, Université, Paris VI, France, 2001, in French.

[4] F. Adenot, Durabilité du béton: Caractérisation et Modélisation des Processus Physiques et Chimiques de Dégradation du Ciment, PhD dissertation, University of Orleans, France, 1992, in French.

[5] M. Mainguy, O. Coussy, Propagation fronts during calcium leaching and chloride penetration, Journal of Engineering Mechanics ASCE 126 (3) (2000) 250–257.

[6] M. Mainguy, F.-J. Ulm, F. Heukamp, Similarity properties of demineralization and degradation of cracked porous materials, International Journal of Solids and Structures 38 (2001) 7079–7100.

[7] M. Mainguy, F.-J. Ulm, Coupled diffusion–dissolution around a fracture channel: the solute congestion phenomenon, Transport in Porous Media 43 (3) (2001, December) 481–497.

[8] H. Saito, S. Nakane, S. Ikari, A. Fujiwara, Preliminary experimental study on the deterioration of cementitious materials by an acceleration method, Nuclear Engineering and Design 138 (1992) 151–155.

[9] B. Gérard, Contribution des couplages mécanique-chimie-transfert duns la tenue à long terme des ouurages de stockage des déchets radioactifs, PhD dissertation, ENS Cachan, France, 1996, in French.

[10] C. Carde, R. Francois, J. Torrenti, Leaching of both calcium hydroxide and C–S–H from cement paste: modeling the mechanical behavior, Cement and Concrete Research 26 (8) (1996) 1257–1268.

[11] P. Mason, The effects of aggressive water on dam concrete, Construction and Building Materials 4 (3) (1990) 17–26.

[12] F. Wittmann, A. Gerdes, Korrosion zementgebundener Werkstoffe unter dem Einfluss eines elektrischen Feldes, Internationale Zeitschrift fuer Bauinstandsetzen 2 (6) (1986) 455–480.

[13] U. Schneider, S.-W. Chen, The chemomechanical effect and the mechanochemical effect on high-performance concrete subjected to stress corrosion, Cement and Concrete Research 28 (4) (1998) 509–522.

[14] C. Le Bellégo, Couplages chimie-mécanique duns les structures en béton attaquées par l'eau: étude expérimentale et analyse numérique, PhD dissertation, ENS Cachan, France, 2001, in French.

[15] F.-J. Ulm, J.-M. Torrenti, F. Adenot, Chemoporoplasticity of calcium leaching in concrete, Journal of Engineering Mechanics ASCE (1999) 1200–1211.

[16] F. Heukamp, F.-J. Ulm, J. Germaine, Mechanical properties of calcium leached cement pastes: triaxial stress states and the influence of the pore pressure, Cement and Concrete Research 31 (5) (2001) 767–774.

[17] B. Bourdette, Durabilité du mortier: Prise en compte des auréoles de transition dans la caractérisation et la modélisation des processus physiques et chimiques d'altération, PhD dissertation, INSA Toulouse, France, 1994, in French.

[18] P. Stutzman, J. Clifton, Specimen preparation for scanning electron microscopy, in: L. Jany, A. Nisperos (Eds.), Proc. 21st Int. Conference on Cement Microscopy, 1999, Las Vegas.

[19] T. Sheahan, J. Germaine, Computer automation of conventional triaxial equipment, ASTM Geotechnical Testing Journal 15 (4) (1992) 311–322.
[20] O. Coussy, Mechanics of Porous Continua, Wiley, Chichester, 1995.
[21] V. Baroghel-Bouny, Caractérisation des pâtes de ciment et des bétons. Méthodes, analyse, interprétations, PhD dissertation, ENPC, France, 1994, Published as LCPC Research Report ref. CARPAT, 1995, in French.
[22] H. Taylor, Cement Chemistry, 2nd ed., Thomas Telford, London, 1997.
[23] A. Schofield, P. Wroth, Critical State Soil Mechanics, McGraw-Hill, New York, 1968.
[24] F.-J. Ulm, F. Heukamp, J. Germaine, Residual design strength of cement-based materials for nuclear waste storage systems, Nuclear Engineering and Design 211 (2002) 51–60.
[25] P. Faucon, F. Adenot, J. Jacquinot, J. Petit, R. Cabrillac, M. Jorda, Long-term behaviour of cement pastes used for nuclear waste disposal: review of physio-chemical mechanisms of water degradation, Cement and Concrete Research 28 (6) (1998) 847–857.
[26] R.-M. Pellenq, A. Delville, H. van Damme, Cohesive and swelling behaviour of charged interfaces: a (N,V,T) Monte-Carlo study, in: B. Enaney, I. Mays, J. Rouquerol, F. Rodriguez-Reinos, K. Sing, K. Kung (Eds.), Characterization of Porous Solids, vol. IV, Royal Society of Chemistry, London, 1997, pp. 596–603.
[27] P. de Buhan, L. Dormieux, On the validity of the effective stress concept for assessing the strength of saturated porous materials: a homogenization approach, Journal of the Mechanics and Physics of Solids 44 (10) (1996) 1649–1667.
[28] A. Bishop, D. Henkel, The Measurement of Soil Properties in the Triaxial Test, 2nd ed., Edward Arnold, London, 1962.
[29] K. Terzaghi, Theoretical Soil Mechanics, J. Wiley, New York, 1943.
[30] H. Hencky, Ueber die Form des Elastizitaetsgesetzes bei ideal elastischen Stoffen, Zeitschrift fuer Technische Physik 9 (457) (1928) 215–220.